Journal of Advanced Ceramics
2018, 7(3): 229–236
https://doi.org/10.1007/s40145-018-0274-4
ISSN 2226-4108
CN 10-1154/TQ

Research Article

Physical and mechanical properties of hot-press sintering ternary CM_2A_8 ($CaMg_2Al_{16}O_{27}$) and $C_2M_2A_{14}$ ($Ca_2Mg_2Al_{28}O_{46}$) ceramics

Bin LI[a,b], Guangqi LI[c], Haiyang CHEN[d], Junhong CHEN[a,*], Xinmei HOU[b,*], Yong LI[a]

[a]*School of Materials Science and Engineering, University of Science and Technology Beijing, Beijing 100083, China*
[b]*Collaborative Innovation Center of Steel Technology, University of Science and Technology Beijing, Beijing 100083, China*
[c]*Shandong Shengchuan Ceramics Co., Ltd., Shandong 255100, China*
[d]*School of Architecture and Construction, Hebei University of Architecture, Zhangjiakou 075000, China*

Received: February 24, 2018; Revised: March 23, 2018; Accepted: March 28, 2018

Abstract: The new ternary CM_2A_8 ($CaMg_2Al_{16}O_{27}$) and $C_2M_2A_{14}$ ($Ca_2Mg_2Al_{28}O_{46}$) pure and dense ceramics were first prepared by a hot-press sintering technique, and their physical and mechanical properties were investigated. The purity of obtained CM_2A_8 and $C_2M_2A_{14}$ ceramics reaches 98.1 wt% and 97.5 wt%, respectively. Their microstructure is dense with few observable pores, and their grain size is about a few dozen microns. For their physical properties, the average apparent porosity of CM_2A_8 and $C_2M_2A_{14}$ ceramics is 0.18% and 0.13%, and their average bulk density is 3.66 g/cm^3 and 3.71 g/cm^3, respectively. The relative density of CM_2A_8 ceramic is 98.12% and that of $C_2M_2A_{14}$ ceramic is 98.67%. The thermal expansivity (50–1400 ℃) of CM_2A_8 and $C_2M_2A_{14}$ ceramics is 9.24×10^{-6} K^{-1} and 8.92×10^{-6} K^{-1}, respectively. The thermal conductivity of CM_2A_8 and $C_2M_2A_{14}$ ceramic is 21.32 W/(m·K) and 23.25 W/(m·K) at 25 ℃ and 18.76 W/(m·K) and 19.42 W/(m·K) as temperature rises to 350 ℃, respectively. In addition, the mechanical properties are also achieved. For CM_2A_8 ceramic, the flexural strength is 248 MPa, the fracture toughness is 2.17 MPa·m$^{1/2}$, and the Vickers hardness is 12.26 GPa. For $C_2M_2A_{14}$ ceramic, the flexural strength is 262 MPa, the fracture toughness is 2.23 MPa·m$^{1/2}$, and the Vickers hardness is 12.95 GPa.

Keywords: hot-press sintering; CM_2A_8; $C_2M_2A_{14}$; physical properties; mechanical properties

1 Introduction

$CaAl_{12}O_{19}$ (CA_6) is a stable calcium aluminate phase with highest Al_2O_3 content in the $CaO–Al_2O_3$ binary system [1–3]. Its theoretical density is 3.79 g/cm^3 and melting point is 1875 ℃ [4–6]. CA_6 has similar thermal expansivity with corundum, low wettability against melting metal and slag, and it is chemically stable in reduction atmosphere (CO) and alkali conditions [7–11]. In recent years, CA_6 has attracted wide attention and been widely applied in steel, petrochemical, and aluminum industry refractories

* Corresponding authors.
E-mail: J. Chen, cjh2666@126.com;
X. Hou, houxinmeiustb@ustb.edu.cn

[12–14]. $MgAl_2O_4$ (MA) is the only stable compound in the $MgO–Al_2O_3$ system with the melting point of 2135 ℃. It is featured with low thermal expansivity, better thermal conductivity, and outstanding mechanical properties, etc. [15–22], and widely used in ladle, cement rotary kiln, and RH refining furnace refractories.

Göbbels *et al.* [23–26] found two ternary compounds in the Al-rich part of $CaO–Al_2O_3–MgO$ system: $CaMg_2Al_{16}O_{27}$ and $Ca_2Mg_2Al_{28}O_{46}$ (abbreviated as CM_2A_8 and $C_2M_2A_{14}$ in the following), which have magnetoplumbite related structures composed of two kinds of structure units, namely M ($CaAl_{12}O_{19}$, magnetoplumbite unit) and S ($MgAl_2O_4$, spinel unit). They also confirmed that the stacking sequences are $(MS)_n$ and $(M_2S)_n$ for CM_2A_8 and $C_2M_2A_{14}$, respectively. In both cases, Mg^{2+} enters CA_6 lattice, rather than causing the structural alteration, but it is stored in CA_6 lattice in the form of magnesium aluminate spinel [25,26]. During the synthesis of CM_2A_8 and $C_2M_2A_{14}$, CA_6 and MA formed initially and then the solid solution reaction occurred between CA_6 and MA to form CM_2A_8 or $C_2M_2A_{14}$ [27]. From the aspect of stacking structure and preparation process, it can be concluded that CM_2A_8 and $C_2M_2A_{14}$ are the composite reaction products of CA_6 and MA at high temperatures. Both CA_6 and MA are excellent refractories which play important roles in many high temperature applications, so it can be deduced that CM_2A_8 and $C_2M_2A_{14}$ are also remarkable refractories which integrate the merits of MA and CA_6. In addition to the higher melting points of CM_2A_8 (1820±10 ℃) and $C_2M_2A_{14}$ (1830±10 ℃) [26], outstanding corrosion resistance was proved by the slag resistance test in our previous work [27]. Besides that, CM_2A_8 and $C_2M_2A_{14}$ can also remove the inclusions in molten steel and purify molten steel, which is due to the M units in their stacking structure. Therefore, CM_2A_8 and $C_2M_2A_{14}$ are promising refractories and expected to be a potential substitute for ladle refining lining in steel industry.

For the preparation and industrial application of refractories, a comprehensive understanding of the physical and mechanical properties of the raw materials is necessary, so as to control the various technique indicators of the refractory product [28–31]. Up to now, CM_2A_8 and $C_2M_2A_{14}$ are only mentioned occasionally in the study of other refractories [32,33], and no specific report on their physical and mechanical properties was carried out. In order to prepare CM_2A_8 and $C_2M_2A_{14}$ series refractories with excellent performance on different application occasions, in this work, the dense CM_2A_8 and $C_2M_2A_{14}$ ceramics were prepared by hot-press sintering and their physical and mechanical properties were investigated, to provide a theoretical basis for the preparation of CM_2A_8 and $C_2M_2A_{14}$ refractories.

2 Experiment process

2. 1 Preparation of CM_2A_8 and $C_2M_2A_{14}$ powders

Analytically pure Al_2O_3, CaO, and MgO (Sinopharm Chemical Reagent Co., Ltd., ω (Al_2O_3) > 98%, ω (CaO) > 99%, ω (MgO) > 98%, average particle size ⩽ 74 μm) were adopted as raw materials in this experiment. In order to accurately quantify, the raw materials were calcinated at 900 ℃ for 1 h to remove the absorbed water and combined water. The batching was conducted with the mass ratio of m(CaO):m(Al_2O_3):m(MgO) = 5.89:85.65:8.46 according to the stoichiometric ratio of CM_2A_8. For $C_2M_2A_{14}$, due to the substitution of Al^{3+} for Mg^{2+} in spinel units of $C_2M_2A_{14}$, the mass ratio of m(CaO):m(Al_2O_3):m(MgO) = 6.94:89.57:3.49 was adopted in accordance with $Ca_2Mg_{2-3x}Al_{28+2x}O_{46}$ as substitution formula and the solid soluble amount x = 0.2 [23,24]. After batching, the raw materials were mixed and wet ball-milled for 48 h (raw materials:balls:water = 1:1.5:2 by mass) and dried at 110 ℃ for 24 h. The mixtures were pressed into bricks and fired at 1750 ℃ for 6 h in air. After free cooling, the CM_2A_8 and $C_2M_2A_{14}$ bricks were taken out, broken, and vibratory-milled, and the as-synthesized powders of CM_2A_8 and $C_2M_2A_{14}$ were obtained.

2. 2 Hot-press sintering process

The as-synthesized powders with an average particle size of less than 74 μm were screened out as raw materials for hot-press sintering. The hot-press sintering was carried out in a cylindrical graphite mould with an inner diameter of 60 mm, in which graphite paper was inserted between powder compacts and the inner wall of graphite mould. The CM_2A_8 and $C_2M_2A_{14}$ powders were pressed into the graphite mould and hot-press sintered. The hot-press sintering procedure is detailed in Fig. 1. The pressure started at 1400 ℃ and increased linearly as the temperature rising; when the temperature was 1750 ℃, the pressure reached the maximum value of 15 MPa. The pressure of 15 MPa remained for

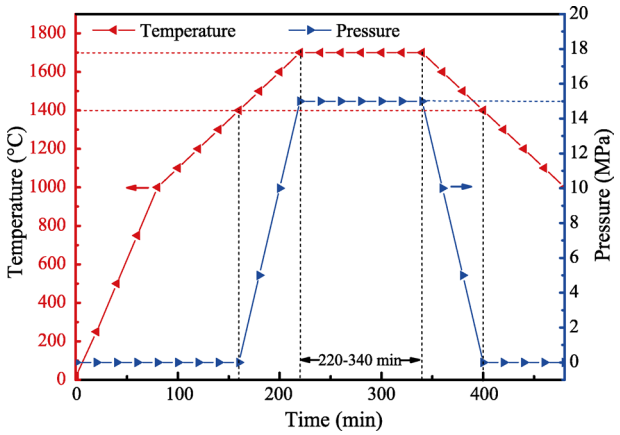

Fig. 1 Diagram of hot-press sintering procedure.

120 min (from 220 to 340 min) at 1750 ℃, and then reduced linearly as the temperature decreased. When the temperature was 1400 ℃, the pressure dropped to 0 MPa. After cooling, the CM_2A_8 and $C_2M_2A_{14}$ ceramics were obtained.

2. 3 Phase and morphology characterization

The phases and morphology were investigated by X-ray diffraction with Cu Kα radiation and a scanning speed of 10 (°)/min (XRD, D8 Advance, Bruker, America) and a scanning electron microscope (SEM, nova^{TM} nano SEM 450, FEI, America) equipped with an energy dispersive spectrometer (EDS, TEAM™, EDAX, America). The obtained ceramics were characterized by transmission electron microscopy (TEM) and selected area electron diffraction (SAED, JEM-1400, JEOL, Japan). The relative contents of the identified phases were obtained by standard less quantitative phase analysis using the TOPAS 5.0 software (Bruker AXS, America) implementing the Rietveld method.

2. 4 Physical and mechanical property tests

The apparent porosity and bulk density of the obtained samples were measured by Archimedes method. The true density was measured by using a pyknometer method. The obtained sample was prepared into the cylinders with diameter of 4 mm and length of 10 mm, and the thermal expansivity tests were conducted by thermal dilatometer (DIL805A, BÄHR-Thermoanalyse GmbH, Germany) with the heating rate of 5±1 ℃/min from 50 to 1400 ℃. The thermal conductivity tests at 25 and 300 ℃ were conducted by laser-flash method (LFA 457 MicroFlash, NETZSCH, Germany) in which 10 mm × 10 mm × 5 mm test pieces were applied. The flexural strength was determined by the three-point bending method, in which 3 mm × 4 mm × 36 mm test pieces were applied with a span of 30 mm and a cross head speed of 0.05 mm/min. The fracture toughness was obtained by the single-edge notched beam (SENB) method, in which 2 mm × 4 mm × 30 mm test pieces were applied with a cross head speed of 0.05 mm/min. The hardness was measured by Vickers indentation with a load of 200 N. The physical and mechanical property measurements were measured 5 times to calculate an average value and standard deviation.

3 Results and discussion

3. 1 Phases and morphology

XRD patterns of CM_2A_8 and $C_2M_2A_{14}$ bricks and ceramics are shown in Fig. 2. As shown in Fig. 2(a), the main phase of CM_2A_8 brick is CM_2A_8, with trace

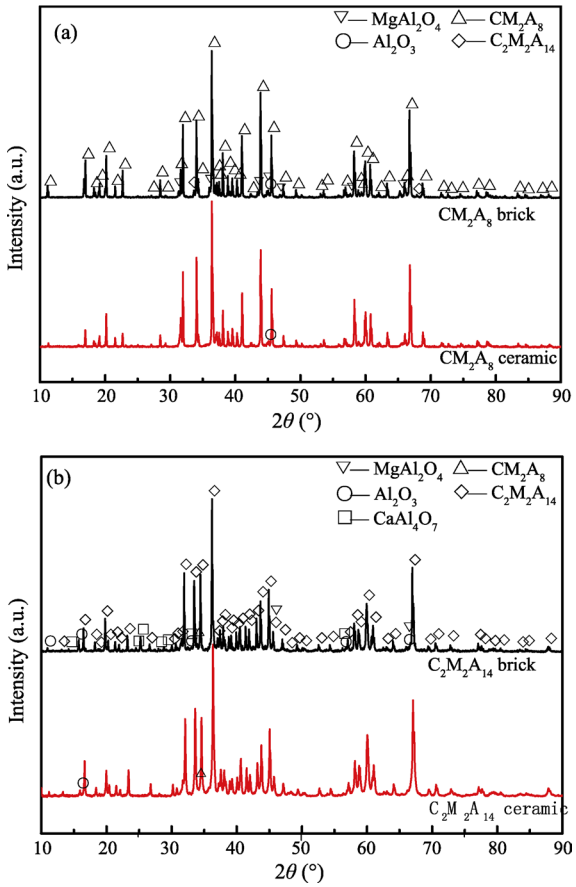

Fig. 2 XRD patterns of CM_2A_8 and $C_2M_2A_{14}$ bricks and ceramics: (a) CM_2A_8 brick and ceramic, (b) $C_2M_2A_{14}$ brick and ceramic.

detectable $C_2M_2A_{14}$, Al_2O_3, and $MgAl_2O_4$. After the hot-press sintering, the main phase of CM_2A_8 ceramic is still CM_2A_8. Those traces $C_2M_2A_{14}$ and $MgAl_2O_4$ disappear, whereas with only Al_2O_3 is remained. However, the peak intensity of Al_2O_3 decreases. As shown in Fig. 2(b), the main phase of $C_2M_2A_{14}$ brick is $C_2M_2A_{14}$, a small amount of CM_2A_8, Al_2O_3, $MgAl_2O_4$, and $CaAl_4O_7$ exist in $C_2M_2A_{14}$ brick. After the hot-press sintering, the main phase of $C_2M_2A_{14}$ ceramic has not changed, and the characteristic peaks of $CaAl_4O_7$ and $MgAl_2O_4$ can no longer be observed. Meanwhile the characteristic peaks of CM_2A_8 and Al_2O_3 can still be observed, but the intensity is reduced.

Rietveld refinement using the XRD data by TOPAS 5.0 software allows to carefully determine the content of each phase. Figure 3 shows an example of Rieveld refined pattern of CM_2A_8 ceramic where well-fitting between the computed pattern (red cross) and the experimental pattern (black line) could be achieved; the blue line is the difference between the experimental data and computed data. The weighted residual factor (R_{wp}, %) and sigma value (S) for CM_2A_8 ceramic were 14.33% and 1.87, respectively. For all the Rietveld refinements in this work, the two important refinement parameters of the TOPAS 5.0 program, weighted residual factor (R_{wp}, %) and sigma value (S), were in the range of 8.35%–14.96% and 1.22–1.92, respectively, indicating reliable Rietveld refinements.

The quantitative analysis results of CM_2A_8 and $C_2M_2A_{14}$ bricks and ceramics by the Rietveld refinement method are shown in Table 1. After the hot-press sintering, the contents of impurities decrease and the purity of CM_2A_8 and $C_2M_2A_{14}$ ceramics is improved.

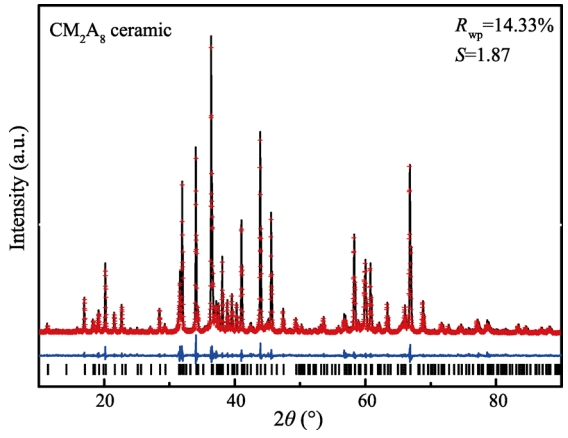

Fig. 3 Rietveld refinement of CM_2A_8 ceramic. The red cross: computed pattern; black line: experimental data.

Table 1 Quantitative analysis results of CM_2A_8 and $C_2M_2A_{14}$ bricks and ceramics (Unit: wt%)

Phase	$C_2M_2Al_{14}$	CM_2A_8	$CaAl_4O_7$	Al_2O_3	$MgAl_2O_4$
CM_2A_8 brick	1.5	94.2	—	2.6	1.7
CM_2A_8 ceramic	—	98.1	—	1.9	—
$C_2M_2A_{14}$ brick	94.3	1.2	1.1	2.3	1.1
$C_2M_2A_{14}$ ceramic	97.5	0.9	—	1.6	—

The purity of CM_2A_8 ceramic reaches 98.1 wt%, and the only 1.9 wt% of Al_2O_3 is found. The purity of $C_2M_2A_{14}$ ceramic is 97.5 wt% with 0.9 wt% of CM_2A_8 and 1.6 wt% of Al_2O_3 as impurities.

SEM images of CM_2A_8 and $C_2M_2A_{14}$ bricks and ceramics, and TEM images and SAED results of CM_2A_8 and $C_2M_2A_{14}$ ceramics are shown in Fig. 4. Table 2 lists the EDS results of CM_2A_8 and $C_2M_2A_{14}$ ceramics. Figures 4(a) and 4(b) exhibit the SEM images of the fracture of CM_2A_8 and $C_2M_2A_{14}$ bricks, respectively. The granular crystal morphology belongs to CM_2A_8 (Fig. 4(a)) and the thick flake crystals are $C_2M_2A_{14}$ (Fig. 4(b)). Many pores can be observed among the grains, and the whole microstructure of synthesized CM_2A_8 and $C_2M_2A_{14}$ bricks is loose. The particle size of crystals in CM_2A_8 and $C_2M_2A_{14}$ bricks is mostly below 10 μm, and large grains and small grains distribute uniformly, gathering together to form the basic microstructure. The SEM images of the fracture of CM_2A_8 and $C_2M_2A_{14}$ ceramics are shown in Figs. 4(c) and 4(d), respectively. After the hot-press sintering, the whole microstructure of CM_2A_8 and $C_2M_2A_{14}$ ceramics is very dense and few pores exist. The particle size of crystals in CM_2A_8 and $C_2M_2A_{14}$ ceramics is about a few dozen microns, and the grains are tightly sintered together. The characteristic morphology of granular crystal for CM_2A_8 and thick flake crystal for $C_2M_2A_{14}$ has not been detected in both CM_2A_8 and $C_2M_2A_{14}$ ceramics. The EDS results (Table 2) of point A in Fig. 4(c) and point B in Fig. 4(d) demonstrate that the atomic ratio of Ca:Mg:Al is about 1:2:16 in CM_2A_8 ceramic and the atomic ratio of Ca:Mg:Al is about 1:1:14 in $C_2M_2A_{14}$ ceramic. The

Table 2 EDS results of the points in Fig. 4

Atomic percent of chemical elements (at%)				
Point	Ca	Mg	Al	O
A	3.05	5.44	40.61	50.90
B	3.59	3.32	40.54	52.55

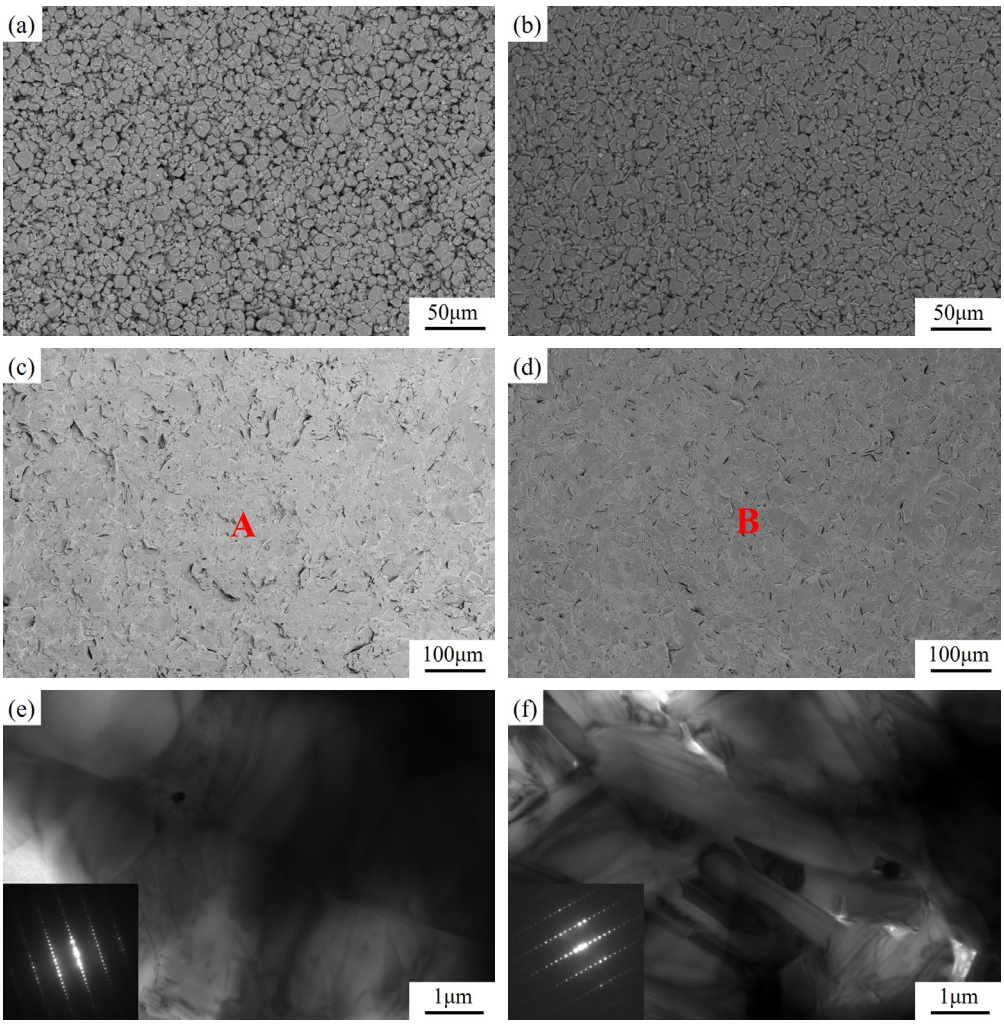

Fig. 4 SEM images of CM_2A_8 and $C_2M_2A_{14}$ bricks and ceramics, and TEM images and SAED results of CM_2A_8 and $C_2M_2A_{14}$ ceramics. (a) SEM image of CM_2A_8 brick; (b) SEM image of $C_2M_2A_{14}$ brick; (c) SEM image of CM_2A_8 ceramic; (d) SEM image of $C_2M_2A_{14}$ ceramic; (e) TEM image and SAED result of CM_2A_8 ceramic; (f) TEM image and SAED result of $C_2M_2A_{14}$ ceramic.

CM_2A_8 and $C_2M_2A_{14}$ ceramics are further characterized by TEM and SAED, as shown in Figs. 4(e) and 4(f). The dense microstructure can be observed from the TEM image, and the SAED results confirm the component of CM_2A_8 and $C_2M_2A_{14}$ ceramics are CM_2A_8 and $C_2M_2A_{14}$, respectively, which are consistent with the results of XRD.

3. 2 Physical properties

Table 3 demonstrates the average apparent porosity, bulk density, and true density of CM_2A_8 and $C_2M_2A_{14}$ bricks and ceramics. The average apparent porosity, bulk density of CM_2A_8 brick are 36.54% and 2.57 g/cm^3 respectively with standard deviation of 2.51% and 0.24 g/cm^3, and that of $C_2M_2A_{14}$ brick are 27.32% and 2.63 g/cm^3 with standard deviation of 3.46% and 0.18 g/cm^3. After the hot-press sintering, the average apparent porosity CM_2A_8 and $C_2M_2A_{14}$ ceramics is greatly reduced to 0.18% and 0.13% with the same standard deviation of 0.02%; meanwhile the bulk density of CM_2A_8 and $C_2M_2A_{14}$ ceramics is increased

Table 3 Average apparent porosity, bulk density, and true density of CM_2A_8 and $C_2M_2A_{14}$ bricks and ceramics

	Apparent porosity (%)	Bulk density (g/cm^3)	True density (g/cm^3)	Theoretical density (g/cm^3)	Relative density (%)
CM_2A_8 brick	36.54±2.51	2.57±0.24	—	—	—
$C_2M_2A_{14}$ brick	27.32±3.46	2.63±0.18	—	—	—
CM_2A_8 ceramic	0.18±0.02	3.66±0.02	3.69±0.01	3.73	98.12
$C_2M_2A_{14}$ ceramic	0.13±0.02	3.71±0.01	3.74±0.01	3.76	98.67

to 3.66 g/cm^3 with standard deviation of 0.02 g/cm^3 and 3.71 g/cm^3 with standard deviation of 0.01 g/cm^3, respectively. By using the pyknometer method, the true density of CM_2A_8 and $C_2M_2A_{14}$ ceramics is 3.69 g/cm^3 and 3.74 g/cm^3 with the same standard deviation of 0.01 g/cm^3. Theoretical density is derived from crystal structure referring to the PDF card database (PDF Card No. 01-086-0383 for CM_2A_8 and PDF Card No. 01-086-0382 for $C_2M_2A_{14}$) [23,24]. The theoretical density of CM_2A_8 and $C_2M_2A_{14}$ ceramics is 3.73 g/cm^3 and 3.76 g/cm^3, respectively. The ratio of bulk density to theoretical density is defined as the relative density which is used to describe the degree of densification of ceramics. The CM_2A_8 and $C_2M_2A_{14}$ ceramics both achieve higher relative density. The relative density of CM_2A_8 ceramic is 98.12% and that of $C_2M_2A_{14}$ ceramic is 98.67%. Combined with the quantitative results of XRD (Table 1), the CM_2A_8 and $C_2M_2A_{14}$ ceramics have high purity and relative density, so their physical and mechanical properties are close to the theoretical value.

Thermal expansivity (50–1400 ℃) and thermal conductivity (at 25 ℃ and 350 ℃) of CM_2A_8 and $C_2M_2A_{14}$ ceramics are shown in Table 4. The thermal expansivity (50–1400 ℃) of CM_2A_8 ceramic is about 9.24×10^{-6} K^{-1} with standard deviation of 0.11×10^{-6} K^{-1}, and that of $C_2M_2A_{14}$ ceramic is 8.92×10^{-6} K^{-1} with standard deviation of 0.14×10^{-6} K^{-1}, both are close to the thermal expansivity of corundum [34] and calcium hexaluminate [35,36]. The thermal expansivity of $C_2M_2A_{14}$ ceramic is slightly less than that of CM_2A_8 ceramic. The thermal conductivity of CM_2A_8 ceramic is 21.32 W/(m·K) with standard deviation of 0.21 W/(m·K) at 25 ℃ and 18.76 W/(m·K) with standard deviation of 0.32 W/(m·K) at 350 ℃. The thermal conductivity of $C_2M_2A_{14}$ ceramic is 23.25 W/(m·K) with standard deviation of 0.18 W/(m·K) at 25 ℃ and 19.42 W/(m·K) with standard deviation of 0.36 W/(m·K) at 350 ℃. Both at 25 ℃ and 350 ℃, the thermal conductivity of CM_2A_8 ceramic is slightly lower than that of $C_2M_2A_{14}$ ceramic. The higher thermal conductivity of $C_2M_2A_{14}$ ceramic may be due to its higher density and lower apparent porosity relative to CM_2A_8.

Table 4 Thermal properties of CM_2A_8 and $C_2M_2A_{14}$ ceramics

	Thermal expansivity (10^{-6}K^{-1}, 50–1400 ℃)	Thermal conductivity (W/(m·K), 25 ℃)	Thermal conductivity (W/(m·K), 350 ℃)
CM_2A_8 ceramic	9.24±0.11	21.32±0.21	18.76±0.32
$C_2M_2A_{14}$ ceramic	8.92±0.14	23.25±0.18	19.42±0.36

3.3 Mechanical properties

Room-temperature mechanical properties of CM_2A_8 and $C_2M_2A_{14}$ ceramics are shown in Table 5. The flexural strength of CM_2A_8 ceramic is 248 MPa with standard deviation of 64 MPa and that of $C_2M_2A_{14}$ ceramic is 262 MPa with standard deviation of 18 MPa. The CM_2A_8 and $C_2M_2A_{14}$ ceramics exhibit similar fracture toughness and Vickers hardness. For CM_2A_8 ceramic, the fracture toughness is 2.17 MPa·m$^{1/2}$ with standard deviation of 0.12 MPa·m$^{1/2}$ and the Vickers hardness is 12.26 GPa with standard deviation of 0.52 GPa. For $C_2M_2A_{14}$ ceramic, the fracture toughness is 2.23 MPa·m$^{1/2}$ with standard deviation of 0.13 MPa·m$^{1/2}$ and the Vickers hardness is 12.95 GPa with standard deviation of 0.73 GPa. In general, the mechanical performance of $C_2M_2A_{14}$ ceramic is slightly better than that of CM_2A_8 ceramic. Higher relative density may be the reason for better mechanical properties of $C_2M_2A_{14}$ ceramic.

The mechanical properties of other commercial refractory materials are show in Table 6. From Tables 5 and 6, the mechanical properties of CM_2A_8 and $C_2M_2A_{14}$ ceramics are similar to that of these commercial refractory materials; especially for the flexural strength, the difference is very small. Due to the good mechanical properties and the function of purifying molten steel, CM_2A_8 and $C_2M_2A_{14}$ are promising refractory materials

Table 5 Mechanical properties of CM_2A_8 and $C_2M_2A_{14}$ ceramics

	Flexural strength (MPa)	Fracture toughness (MPa·m$^{1/2}$)	Vickers hardness (GPa)
CM_2A_8 ceramic	248±64	2.17±0.12	12.26±0.52
$C_2M_2A_{14}$ ceramic	262±18	2.23±0.13	12.95±0.73

Table 6 Mechanical properties of other commercial refractory materials

	Flexural strength (MPa)	Fracture toughness (MPa·m$^{1/2}$)	Vickers hardness (GPa)
Al_2O_3 (corundum)	135–210 [37]	3.46–4.21 [37]	15 [38]
$MgAl_2O_4$ (spinel)	241 [39]	1.72±0.06 [39]	9.36 [38]
MgO	250 [40]	2.79 [41]	12.2 [40]

and expected to be applied in ladle refining lining in steel industry.

4 Conclusions

The new ternary CM_2A_8 and $C_2M_2A_{14}$ pure and dense ceramics in the Al-rich part of $CaO–Al_2O_3–MgO$ system were first prepared by hot-press sintering. Their physical and mechanical properties were investigated. After the hot-press sintering, the purity of obtained CM_2A_8 ceramic reaches 98.1 wt%, and that of $C_2M_2A_{14}$ ceramic is 97.5 wt%. The microstructure of CM_2A_8 and $C_2M_2A_{14}$ ceramics are very dense and few pores exist. The grains of CM_2A_8 and $C_2M_2A_{14}$ ceramics which exhibit a particle size of about a few dozen microns are tightly sintered together. The characteristic morphology of granular crystal for CM_2A_8 and thick flake crystal for $C_2M_2A_{14}$ has not been detected in both CM_2A_8 and $C_2M_2A_{14}$ ceramics.

Their physical properties were measured. The average apparent porosity of CM_2A_8 and $C_2M_2A_{14}$ ceramics is 0.18% and 0.13%, and their average bulk density is 3.66 g/cm^3 and 3.71 g/cm^3, respectively. The relative density of CM_2A_8 ceramic is 98.12% and that of $C_2M_2A_{14}$ ceramic is 98.67%. The thermal expansivity (50–1400 ℃) of CM_2A_8 ceramic is 9.24×10^{-6} K^{-1}, and that of $C_2M_2A_{14}$ ceramic is 8.92×10^{-6} K^{-1}. The thermal conductivity of CM_2A_8 and $C_2M_2A_{14}$ ceramic is 21.32 W/(m·K) and 23.25 W/(m·K) at 25 ℃ and 18.76 W/(m·K) and 19.42 W/(m·K) as temperature rises to 350 ℃, respectively.

For the mechanical properties, the flexural strength of CM_2A_8 ceramic is 248 MPa and that of $C_2M_2A_{14}$ ceramic is 262 MPa. For CM_2A_8 ceramic, the fracture toughness is 2.17 MPa·m$^{1/2}$ and the Vickers hardness is 12.26 GPa. For $C_2M_2A_{14}$ ceramic, the fracture toughness is 2.23 MPa·m$^{1/2}$ and the Vickers hardness is 12.95 GPa.

Acknowledgements

This research was supported by the National Natural Science Foundation of China (No. 51572019) and the National Science Fund for Excellent Young Scholars of China (No. 51522402).

References

[1] Chen J, Chen H, Mi W, *et al.* Substitution of Ba for Ca in the structure of $CaAl_{12}O_{19}$. *J Am Ceram Soc* 2017, **100**: 413–418.

[2] Chen J, Chen H, Yan M, *et al.* Formation mechanism of calcium hexaluminate. *Int J Miner Metall Mater* 2016, **23**: 1225–1230.

[3] Iglesia PGDL, García-Moreno O, Torrecillas R, *et al.* Influence of different parameters on calcium hexaluminate reaction sintering by spark plasma. *Ceram Int* 2012, **38**: 5325–5332.

[4] Yi S, Huang Z, Huang J, *et al.* Novel calcium hexaluminate/spinel-alumina composites with graded microstructures and mechanical properties. *Sci Rep* 2014, **4**: 4333.

[5] Utsunomiya A, Tanaka K, Morikawa H, *et al.* Structure refinement of $CaO·6Al_2O_3$. *J Solid State Chem* 1988, **75**: 197–200.

[6] Park J-G, Cormack AN. Potential models for multicomponent oxides: Hexa-aluminates. *Philos Mag B* 1996, **73**: 21–31.

[7] Domínguez C, Chevalier J, Torrecillas R, *et al.* Thermomechanical properties and fracture mechanisms of calcium hexaluminate. *J Eur Ceram Soc* 2001, **21**: 907–917.

[8] Lister DH, Glasser FP. Phase relations in the system $CaO–Al_2O_3$–iron oxide. *Brit Ceram Soc Trans* 1967, **66**: 293–305.

[9] Tak JB, Young DJ. Sulphur corrosion of calcium aluminate-bonded castables. *Am Ceram Soc Bull* 1982, **61**: 725.

[10] Domínguez C, Chevalier J, Torrecillas R, *et al.* Microstructure development in calcium hexaluminate. *J Eur Ceram Soc* 2001, **21**: 381–387.

[11] Lee WE, Vieira W, Zhang S, *et al.* Castable refractory concretes. *Int Mater Rev* 2001, **46**: 145–167.

[12] Fuhrer M, Hey A, Lee WE. Microstructural evolution in self-forming spinel/calcium aluminate-bonded castable refractories. *J Eur Ceram Soc* 1998, **18**: 813–820.

[13] Chan C-F, Ko Y-C. Effect of CaO content on the hot strength of alumina-spinel castables in the temperature range of 1000° to 1500 ℃. *J Am Ceram Soc* 1998, **81**: 2957–2960.

[14] Tulliani JM, Pagès G, Fantozzi G, *et al.* Dilatometry as a tool to study a new synthesis for calcium hexaluminate. *J Therm Anal Calorim* 2003, **72**: 1135–1140.

[15] Ganesh I, Bhattacharjee S, Saha BP, *et al.* An efficient $MgAl_2O_4$ spinel additive for improved slag erosion and penetration resistance of high-Al_2O_3 and MgO–C refractories. *Ceram Int* 2002, **28**: 245–253.

[16] Baudín C, Martínez R, Pena P. High-temperature mechanical behavior of stoichiometric magnesium spinel. *J Am Ceram Soc* 1995, **78**: 1857–1862.

[17] Braulio MAL, Rigaud M, Buhr A, *et al.* Spinel-containing alumina-based refractory castables. *Ceram Int* 2011, **37**: 1705–1724.

[18] Ko Y-C. Influence of the characteristics of spinels on the slag resistance of Al_2O_3–MgO and Al_2O_3–spinel castables.

J Am Ceram Soc 2000, **83**: 2333–2335.
[19] Sarpoolaky H, Ahari KG, Lee WE. Influence of *in situ* phase formation on microstructural evolution and properties of castable refractories. *Ceram Int* 2002, **28**: 487–493.
[20] Sako EY, Braulio MAL, Brant PO, *et al*. The impact of pre-formed and *in situ* spinel formation on the physical properties of cement-bonded high alumina refractory castables. *Ceram Int* 2010, **36**: 2079–2085.
[21] Ko Y-C. Role of spinel composition in the slag resistance of Al_2O_3–spinel and Al_2O_3–MgO castables. *Ceram Int* 2002, **28**: 805–810.
[22] Aza AHD, Pena P, Rodriguez MA. New spinel-containing refractory cements. *J Eur Ceram Soc* 2003, **23**: 737–744.
[23] Göbbels M, Woermann E, Jung J. The Al-rich part of the system CaO–Al_2O_3–MgO: Part I. Phase relationships. *J Solid State Chem* 1995, **120**: 358–363.
[24] Iyi N, Göbbels M, Matsui Y. The Al-rich part of the system CaO–Al_2O_3–MgO: Part II. Structure refinement of two new magnetoplumbite-related phases. *J Solid State Chem* 1995, **120**: 364–371.
[25] Aza AHD, Pena P, Aza SD. Ternary system Al_2O_3–MgO–CaO: I, primary phase field of crystallization of spinel in the subsystem $MgAl_2O_4$–$CaAl_4O_7$–CaO–MgO. *J Am Ceram Soc* 1999, **82**: 2193–2203.
[26] Aza AHD, Iglesias JE, Pena P, *et al.* Ternary system Al_2O_3–MgO–CaO: Part II, phase relationships in the subsystem Al_2O_3–$MgAl_2O_4$–$CaAl_4O_7$. *J Am Ceram Soc* 2000, **83**: 919–927.
[27] Chen J, Chen H, Mi W, *et al.* Synthesis of CaO·2MgO·8Al_2O_3 (CM_2A_8) and its slag resistance mechanism. *J Eur Ceram Soc* 2017, **37**: 1799–1804.
[28] Mukhopadhyay S, Poddar PKD. Effect of preformed and *in situ* spinels on microstructure and properties of a low cement refractory castable. *Ceram Int* 2004, **30**: 369–380.
[29] Santos WND. Effect of moisture and porosity on the thermal properties of a conventional refractory concrete. *J Eur Ceram Soc* 2003, **23**: 745–755.
[30] Fahrenholtz WG, Hilmas GE, Talmy IG, *et al.* Refractory diborides of zirconium and hafnium. *J Am Ceram Soc* 2007, **90**: 1347–1364.
[31] Koksal F, Gencel O, Brostow W, *et al.* Effect of high temperature on mechanical and physical properties of lightweight cement based refractory including expanded vermiculite. *Mater Res Innov* 2012, **16**: 7–13.
[32] Sako EY, Braulio MAL, Zinngrebe E, *et al.* In-depth microstructural evolution analyses of cement-bonded spinel refractory castables: Novel insights regarding spinel and CA_6 formation. *J Am Ceram Soc* 2012, **95**: 1732–1740.
[33] Sarpoolaky H, Zhang S, Lee WE. Corrosion of high alumina and near stoichiometric spinels in iron-containing silicate slags. *J Eur Ceram Soc* 2003, **23**: 293–300.
[34] Austin JB. The thermal expansion of some refractory oxides. *J Am Ceram Soc* 1931, **14**: 795–810.
[35] Brooksbank D. Thermal expansion of calcium aluminate inclusions and relation to tessellated stresses. *J Iron Steel Inst* 1970, **208**: 495–499.
[36] Criado E, Aza SD. Calcium hexaluminate as refractory material. In Proceedings of the Unified International Technical Conference on Refractories, 1991.
[37] Zhang QC. Fracture toughness and thermal shock behavior of high alumina ceramics. *J Chin Ceram Soc China* 1980, **8**: 223–231.
[38] Zhang SY. Sintering of magnesium aluminate. M.S. Thesis. Xi'an University of Architecture and Technology, 2004.
[39] Yu HX. *Infrared Optical Material.* Beijing, China: National Defend Industry Press, 2007.
[40] Xiao HN, Gao PZ. *High Performance Ceramic and Application.* Beijing, China: Chemical Industry Press, 2006.
[41] Chen Y, Cao LY. *Mechanical Engineering Materials.* Shenyang, China: Northeastern University Press, 2008.